EES Batteries

PAPER

View Article Online
View Journal | View Issue

Cite this: *EES Batteries*, 2026, **2**, 652

Observation of anomalous capacity hysteresis in commercial sodium ion batteries at low temperatures

Harshitha Marikundam,[a] Selva Seelan Margoschis,[a] Patricio Solana Bustamante,[a] Bhumika Bhangale,[a] Kumlachew Zelalem Walle,[b] Linqin Mu,[b] Andrew Weng*[c] and Nicholas Rolston *[a]

We report on a surprising low-temperature phenomenon that is unique to commercial-off-the-shelf (COTS) Na-ion batteries (NIBs) tested in this work, where the capacity hysteresis ratio, defined as charge capacity divided by discharge capacity, exceeds unity. Specifically, we compare degradation behaviors between LIBs (Molicel) and COTS NIBs (Hakadi, $Na_xNiMnFeO_2$|hard carbon|~57% carbonate electrolyte abbreviated as NMF|HC|SC57) at −20 °C, 0 °C, and 20 °C with similar charge/discharge rates at each temperature. At −20 °C, the measured capacity hysteresis ratio is ~207% higher for NIBs; at 0 °C, it is ~60% higher than LIBs. Differential capacity analysis reveals no voltage shifts as a function of temperature in these NIBs unlike LIBs, suggesting unusual kinetics. This behavior exists even under slow cycling, indicating it is not rate limited. To better understand the origins of this behavior, we characterized the positive electrode, negative electrode, and electrolyte components which revealed sodium metal deposition and stable SEI formation on the negative electrode along with excess electrolyte within the battery can. These insights along with the anomalous hysteresis suggests that new physics is needed to fully explain the low-temperature behavior of commercial NIBs.

Received 27th September 2025,
Accepted 4th January 2026

DOI: 10.1039/d5eb00185d

rsc.li/EESBatteries

Broader context

We observe that commercial Na-ion batteries (NIBs) tested so far perform very differently at low temperatures than commercial Li-ion batteries (LIBs). Surprisingly, the charge capacity is ~207% higher than the discharge capacity, a new behavior we term as a "greedy battery". To the best of our knowledge, this behavior of an increased charge capacity well above the rated value has not been reported in any battery. This behavior is one that potentially opens new opportunities for the usage of COTS NIBs. This work motivates additional studies regarding the implications of greedy battery operation, including its effects on battery stability, safety, efficiency and potential practical applications.

1. Introduction

The development of rechargeable batteries has enabled a range of applications, from consumer electronics to electric vehicles (EVs). While LIBs have dominated the market due to their high energy density, NIBs are gaining attention due to their significantly higher abundance and lower costs.[1] NIBs are being explored as a potential solution to address the growing demand for sustainable energy storage in electric vehicles (EVs) and grid-scale energy storage applications.[2,3] However, NIBs are still more nascent in terms of manufacturing technology compared to LIBs. Due to the limited manufacturing capabilities, many fundamental properties are still not well-characterized for COTS NIBs, including cycle life, rate capability, long-term degradation mechanisms and low-temperature performance.[4,5]

Low temperatures lead to increased internal resistance, slower ion transport, and altered electrode–electrolyte interface reactions, ultimately reducing battery efficiency and lifespan.[6] This issue is particularly problematic for EVs, where cold weather can reduce driving range as seen in consumer reports from regions such as Chicago.[7] Recent studies have shown that forming a stable solid-electrolyte interphase (SEI) layer at low temperatures is critical for maintaining the long-term stability of LIBs.[8] However, many LIBs experience poor SEI formation at these temperatures, resulting in irreversible capacity

[a]*Renewable Energy Materials and Devices Lab, School of Electrical, Computer and Energy Engineering (ECEE), Arizona State University, Tempe, AZ, USA. E-mail: nicholas.rolston@asu.edu*
[b]*Materials Science and Engineering, School for Engineering of Matter, Transport, and Energy, Arizona State University, Tempe, USA*
[c]*Department of Mechanical Engineering, University of Michigan, Ann Arbor, MI, USA. E-mail: asweng@umich.edu*

loss and decreased performance over time.[9] Moreover, at low temperatures, reduced ionic conductivity and slower charge transfer kinetics lead to the formation of lithium metal on the negative electrode, which further accelerates capacity fade and increases the risk of short circuits.[10,11] Breakthroughs in electrolyte chemistry have shown promise in addressing some of these low-temperature performance issues. Researchers have developed novel electrolyte formulations to improve ionic conductivity and SEI stability at low temperatures.[12] For example, small-scale studies have demonstrated the effectiveness of low-temperature electrolytes in enhancing LIB performance down to −40 °C.[12–16]

While significant progress has been made in understanding lowtemperature behavior in LIBs, considerably fewer studies have explored the performance of commercial NIBs under similar conditions.[17,18] Despite the importance of low-temperature performance, there is surprisingly little data to answer some basic yet fundamental questions, such as "How does the low-temperature performance of existing commercial NIBs compare to LIBs?" This study offers a comparative study of essential performance benchmarks at low-temperature between commercial NIBs and LIBs. We focus specifically on fundamental performance metrics such as discharge capacities, charge capacities, differential capacity curves, and material properties of the electrodes and electrolyte. We report on a new phenomenon in low-temperature NIB operation, in which the low-temperature charge capacity significantly exceeds the discharge capacity. This observation is explored both phenomenologically and through a mechanistic lens. This work broadly highlights the need for further research to better understand the degradation mechanisms of both LIBs and NIBs at extreme temperatures, particularly in COTS batteries.[19]

2. Methods

2.1. Battery parameters

All batteries for this work were cylindrical cells with a format of 18 650 or 21 700. For battery testing and analysis, we selected one variant for each LIB and NIB. For the LIBs, we selected Molicel INR-21700-P42A[20] with a nominal capacity of 4200 mAh. These cells used a nickel-rich NMC positive electrode and a graphite negative electrode with a rated voltage of 3.6 V. The specified cut-off voltage is 4.2 V for charge and 2.5 V for discharge. For NIBs, we selected the most easily obtainable manufacturer, Hakadi 18650-3V[21] from Selian Energy, with a nominal capacity of 1530 mAh and a nominal voltage of 3 V, and cut-off voltages of 4.1 V for charge and 1.5 V for discharge. The parameters of these cells are shown below in Table S1.

2.2. Battery testing

The batteries for this study were cycled using a Biologic BCS 800 Series battery cycler shown in Fig. S1. Independent channels of BCS-815 with a maximum current of ±15 A per channel and two BCS-810 s that include eight independent channels with a maximum current of ±1.5 A per channel were used for this study. An Associated Environmental Systems SD-508-ATP Environmental Test Chamber was used for the low-temperature degradation experiments. The batteries were connected to the Biologic in a 4-wire configuration where separate leads were used for the current-carrying terminals and the voltage-sensing terminals. This ensures that there is no current passing through the voltage-sensing leads, or connectors, cables, or connection interfaces with the potentiostat, avoiding any potential IR drops or noise. Battery tabbing was performed using a spot welder under controlled conditions (voltage >5 V, delay of 15 seconds, and power of 5 W), ensuring strong and reliable connections between the battery terminals and the alligator clips. Both LIBs and NIBs were cycled under controlled environmental conditions using a Biologic battery cycling system at −20 °C, 0 °C and 20 °C.

The first set of experiments compared the behavior of commercial LIBs and NIBs at extreme low temperature, −20 °C and 20 °C, focusing on the capacity curves. We followed a test protocol as outlined in Table S2. The procedure began with an initial 10-second rest period to record the Open Circuit Voltage (OCV), followed by Potentiostatic Electrochemical Impedance Spectroscopy (PEIS) at a voltage amplitude of 10 mV, then another 10-second rest period was maintained to note the OCV. The battery was then charged using Constant Current (CC) until the voltage limit was reached, followed by Constant Voltage (CV) charging. A 15-minute rest period was introduced afterward to ensure stability, after which PEIS was performed again. Following this, another 15-minute rest period was maintained, and the battery was discharged using Constant Current (CC) to the cutoff voltage. A final 15-minute rest period was then introduced for stabilization before looping the test protocol from Step 1. Note that the PEIS data included in this work were analyzed solely for evaluating resistance, whereas the cycling and electrochemical data was reported and analyzed elsewhere.[22]

The second set of experiments studied battery performance at 0 °C, a more realistic low-temperature operational condition since many COTS batteries are not rated to be charged at −20 °C. We initially performed Reference Performance Tests (RPTs) for both the cells at room temperature with charge/discharge rates as 0.05C/0.2C for the initial capacity check.[23] All cells were tested using the standard protocol of Constant Current (CC) charge, Constant Voltage (CV) charge, and Constant Current (CC) discharge, as outlined in Table 1, for comparative analysis across different temperatures. The test

Table 1 Test configuration for the second set of experiments at 0 °C

Step	Controls
0	Rest
1	Constant Current (CC) charge
2	Constant Voltage (CV) charge
3	Constant Current (CC) discharge
4	Loop to step 1 for >100 cycles

protocol began with an initial rest period of 10 seconds to stabilize the cell, followed by a Constant Current (CC) charge to the cut-off voltage. Then the cells were charged using Constant Voltage (CV) until the current dropped to the specified limit. Finally, the cells were discharged using Constant Current (CC) discharge to their respective cut-off voltages and the test routine is repeated in a loop. There was no rest period between the charge and discharge steps, and the full charge/discharge routine was looped continuously for cycling analysis.

2.3. Battery characterization

2.3.1. Differential capacity. To understand the electrochemical behavior and performance degradation of LIBs and NIBs differential capacity analysis $\left(\frac{dQ}{dV}\right)$[24,25] calculations were performed. The $\frac{dQ}{dV}$ curves were obtained by differentiating the incremental capacity (Q) with respect to voltage (V) for both charge and discharge as shown in eqn (1). This method can be used to indirectly study different phase transitions and chemical changes from ion movement while charging and discharging.

$$\left(\frac{dQ}{dV}\right)_k = \frac{|Q_k - Q_{k-1}|}{|E_k - E_{k-1}|} \quad (1)$$

In eqn (1), Q_k and E_k are the capacity and voltage measured at a given time 'k', while Q_{k-1} and E_{k-1} are the values from previous time step. This analysis allowed us to analyze the shift in peak positions, voltage, or width and provide insights into kinetic limitations, thermodynamic properties, and degradation mechanisms.

2.3.2. Electrochemical impedance spectroscopy (EIS). EIS was analyzed to understand how bulk resistance (R_b), solid electrolyte interface resistance (SEI) (R_{SEI}) and charge transfer resistance (R_{ct}) affect the performance of commercial LIBs and NIBs. Spectra were recorded at selected temperatures and states of charge as outlined in Table S2. The Nyquist plots were fitted in EC Lab (BioLogic)[26] using an equivalent circuit,[27] which is a bulk resistance R_b in series with two parallel resistor-non ideal capacitor (R-CPE) branches, $R_{SEI}\|Q_{CPE}$ and $R_{ct}\|Q_{CPE}$, with a low frequency Warburg element for ion diffusion. Initial parameters were estimated from the high frequency intercept and arc diameters, refined by non-linear least-squares fitting. The extracted R_b, R_{SEI} and R_{ct} values were then compared across temperature for LIBs and NIBs tested.

2.3.3. Gas chromatography mass spectroscopy (GC-MS). Electrolyte samples from NIBs were analyzed to understand their chemical composition using GC-MS (Shimadzu GCMS-QP2050). The analysis focused on the neat (undiluted) electrolyte extracted from the battery. The GC-MS was operated in scan mode over a mass-to-charge (m/z) range of 35–500, with data collected from 1 to 29 minutes. Key instrument parameters included an injection port temperature of 250 °C, a split injection ratio of 1 : 50 and helium (He) as the carrier gas with a constant linear velocity of 40 cm s^{-1}. The oven was program began at 40 °C, held for 3 minutes, increased at a rate of 10 °C min^{-1}, and was held at 250 °C for 5 minutes. The ion source temperature was maintained at 200 °C, and the interface was set to 230 °C. Compounds were identified using the Wiley/NIST 2023 mass spectral library with a match threshold of 75% or greater. This setup allowed for the detection of salts, organic solvents and potential additives present in the COTS NIBs.

3. Results and discussion

3.1. Characterization of cyclability at −20 °C

To understand the low-temperature behavior of COTS batteries, we first compared the extent of capacity fade from charge and discharge profiles at −20 °C and 20 °C. LIBs and NIBs with current rates of 0.375C/0.375C and 1C/1C, respectively, were used in this experiment to probe slower and faster cycling rates. Multiple cells were studied to verify the reproducibility across cycles. As expected, both LIBs and NIBs exhibited a decrease in capacity at −20 °C due to slow kinetics at low temperatures, a common trend in literature.[28]

LIBs showed a ~33% decrease in discharge capacity compared to their rated value (4200 mAh), with an initial measurement of 2790 ± 24.4 mAh. We observed an interesting behavior of a small but repeatable initial increase in discharge capacity over the first five cycles (Fig. 1a). We attribute this to an activation effect comprising the following phenomena: (i) initial stabilization of ion transport pathways with lower resistance, (ii) progressive electrolyte wetting and infiltration of the porous electrodes and (iii) minor relaxation of the electrode and interphase structures.[29] A decline was observed over the following 15 cycles, reaching the average discharge capacity 2220 ± 14.9 mAh by cycle 20 (Fig. 1b). Upon returning to 20 °C, LIBs exhibited partial capacity recovery to ~79% of the rated value of 3310 ± 37.4 mAh as shown in Table 2. NIBs had a mostly similar initial capacity retention at −20 °C with a ~28% decrease relative to the rated value (1530 mAh), measured at 1100 ± 44.3 mAh (Fig. 1c). However, rather than stabilizing, a steady decline was observed over the first 10 cycles with the average discharge capacity decreasing to 761 ± 23.5 mAh by the 20th cycle (Fig. 1d). Similarly, NIBs also showed an ~78% recovery in capacity of 1180 ± 3.97 mAh. But we did not observe the initial capacity rise as seen in LIBs.

Furthermore, comparing the charge capacities, we observe an anomalous phenomenon. LIBs followed the expected behavior, where the discharge capacity was slightly lower than the charge capacity, and their ratios are close to unity. In case of NIBs, however, the charge capacity at −20 °C is ~300% higher than the charge capacity at 20 °C. This result was consistent across four independently tested cells, suggesting the phenomenon is reproducible, *i.e.*, not due to a defective NIB cell. All the results from this dataset were also analyzed in the same way, so the anomaly cannot be due to inconsistencies in data processing methods. We further verified that the experiment was free of test errors. Altogether, we believe this anomalous result represents a physical phenomenon unique to the

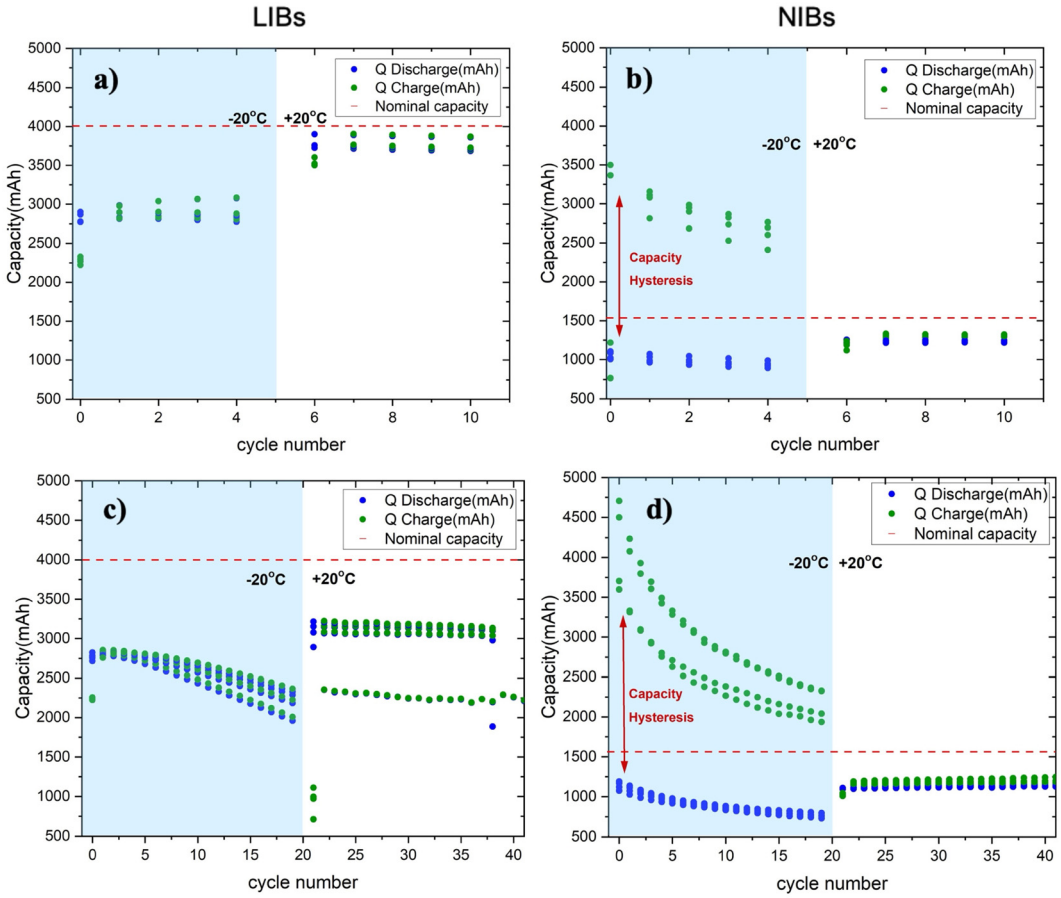

Fig. 1 Capacity curves of LIBs and NIBs cycled at −20 °C followed by 20 °C: (a) LIBs for five cycles (b) NIBs for five cycles (c) LIBs for 20 cycles (d) NIBs for 20 cycles. Capacity hysteresis between charge and discharge cycles is observed for NIBs in (b) & (d). Red dashed line represents the nominal capacities according to the manufacturers.

Table 2 Average discharge capacity of LIB (0.375C/0.375C) and NIB (1C/1C) tested at −20 °C and then 20 °C

Battery	Rated capacity (mAh)	Initial (−20 °C, mAh)	After 5 cycles (−20 °C, mAh)	After 20 cycles (−20 °C, mAh)	Recovery at 20 °C (mAh)
Li	4200	2790 ± 24.4	2885 ± 11.6	2220 ± 14.9	3310 ± 37.4
Na	1530	1100 ± 44.3	937 ± 35.9	761 ± 23.5	1180 ± 3.97

NIB chemistry. This result was unexpected since the cell capacity should decrease monotonically with decreasing temperatures due to kinetic limitations (*i.e.*, ion mobility and charge transfer processes both become hindered at low temperatures). Thus, standard kinetic theories cannot explain this result.[30,31]

3.2. Capacity hysteresis: a phenomenon in NIBs at low temperature

Next, we conducted a second set of experiments at 0 °C under maximum charge/discharge C-rates as specified in their datasheets.[20,21] Again, we observed a large capacity hysteresis of more than 60%, which was not present in the LIBs.

To further quantify the anomalous behavior of charge capacity higher than discharge, we define a capacity hysteresis ratio metric as the average charge capacity divided by the average discharge capacity:

$$\text{Capacity hysteresis ratio} = \text{Avg}\left(\frac{\text{Charge capacity}}{\text{Discharge capacity}}\right) \quad (2)$$

To systematically analyze capacity hysteresis ratios, we jointly analyzed the datasets across all tested temperatures, using the first set of experiments for 20 °C and −20 °C and the second set for 0 °C. The results, shown in Fig. 2a, revealed that the capacity hysteresis in NIBs is a temperature-dependent phenomenon; the hysteresis ratio grows larger with decreasing temperatures. Specifically, at 20 °C, the hysteresis ratio is close to unity, as expected. However, at 0 °C this ratio grows to 1.6 ± 0.08 and further to 3.37 ± 1.2 by −20 °C during cycle 1. With continued cycling, the hysteresis further increases by 80%

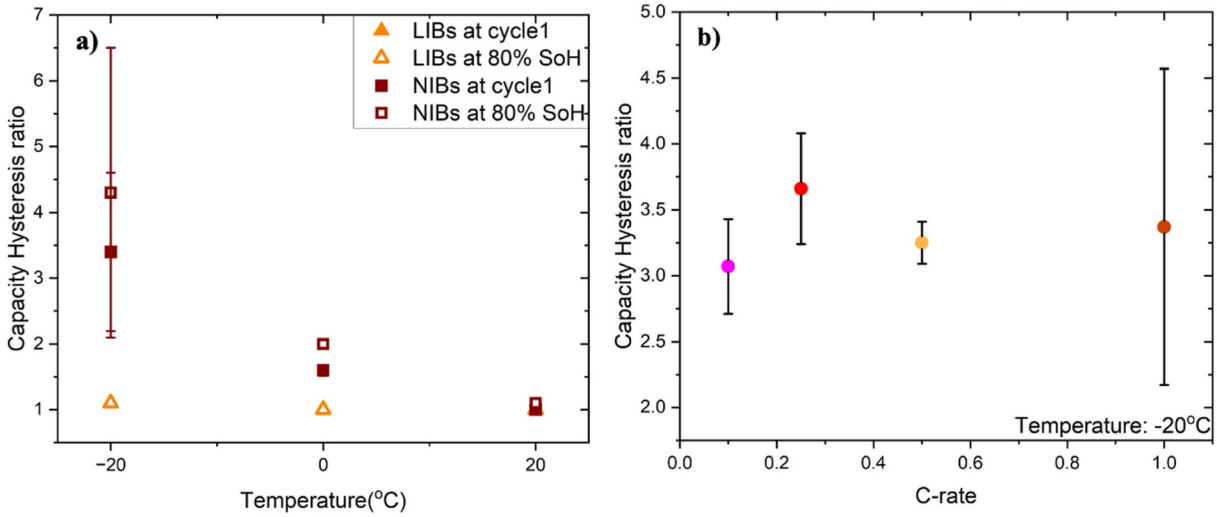

Fig. 2 Capacity hysteresis ratios for: (a) LIBs and NIBs measured at −20 °C, 0 °C and 20 °C during the first cycle and at 80% SoH. The data highlights the low-temperature dependence on capacity hysteresis for NIBs. (b) NIBs at −20 °C for different C-rates.

state of health (SoH), the hysteresis ratios reach 2.00 ± 0.06 at 0 °C and 4.30 ± 2.2 at −20 °C. In contrast, LIBs showed much lower capacity hysteresis ratios, with values close to unity across all temperatures and cycles of 1.10 ± 0.00 at −20 °C, 1.00 ± 0.00 at 0 °C, and 1.00 ± 0.00 at 20 °C. LIB capacity hysteresis ratios also did not significantly change after aging, maintaining their values close to unity even at 80% SoH. The temperature-dependent capacity hysteresis phenomenon thus occurs exclusively in the NIB chemistry.

We next evaluated the effect of charge and discharge C-rates on the capacity hysteresis ratios in NIBs. Specifically, cells were cycled at −20 °C using a range of lower cycling rates of 0.5C/0.5C, 0.25C/0.25C and 0.1C/0.1C charge/discharge rates. In all cases, the capacity hysteresis ratio far exceeded unity, showing a similar trend observed in Fig. 1. Even with the reduced C-rates, which typically allow for more ion transport and less kinetic limitations, the capacity hysteresis remained in a relatively comparable range (Fig. 2b). The presence of the large capacity hysteresis ratios even at lower C-rates suggests that the anomalous charge capacity may have a thermodynamic origin rather than being a purely kinetic effect.

3.3. Differential capacity analysis of LIBs and NIBs

We performed differential capacity analysis $\left(\frac{dQ}{dV}\right)$ of LIBs and NIBs, comparing trends across cycles and across temperatures. First, considering different cycles with temperature held at 20 °C, LIBs exhibited sharp, symmetric, and distinct peaks while charging and discharging for the voltage range ~(3.4–4.2) V (Fig. 3a). These features are a characteristic of stable and reversible intercalation/deintercalation processes in LIBs with NMC positive electrode and graphite negative electrodes. The cathodic $\left(\frac{dQ}{dV}\right)$ corresponds to phase transitions between hexagonal structures to monoclinic (H1 ↔ M ↔ H2 ↔ H3) in the layered NMC corresponding at each peak. On the graphite side, peaks correspond to staging transition mechanism such as $LiC_6 \leftrightarrow LiC_{12}$.[32–34] In contrast, NIBs exhibited broad and less defined peaks, with peaks observed during charging within the voltage range of ~(2.5–4) V and during discharging within ~(2.4–2.7) V[16] (Fig. 3d). This asymmetry in NIBs is not surprising based on the different electrodes used and suggests distinct reaction mechanisms. The NMF positive electrode likely undergoes Na^+ intercalation/deintercalation through multiple transition metal redox. Specifically, the main sharp peaks (1) are attributed to Ni^{2+}/Ni^{3+} redox couple interacting with hard carbon, while the broader peaks (2) correspond to Ni^{3+}/Ni^{4+} and Fe^{2+}/Fe^{3+} redox activity.[35,36] These redox processes are also typically accompanied by structural changes in layered oxide positive electrodes such as O3 ↔ P3 phase transitions during cycling.[37] The repeatability of the peak features across tens of cycles confirms that these features are indeed related to ion insertion and extraction.

As the operating temperature is successively lowered from room temperature to 0 °C and then to −20 °C, the asymmetry in differential capacity features becomes amplified (Fig. 3b, c, e and f). During charging, the peaks are pushed towards higher voltages, and during discharging, the peaks are pushed towards lower voltages. This low-temperature peak separation occurs for both LIBs and NIBs, though the effect is more pronounced for NIBs. For NIBs, although detailed studies of the specific chemistry at low temperatures remain limited, the unusually sharp peak ~(3–4) V and the loop observed at −20 °C (Fig. 3e and f) are not commonly reported. One possible explanation is the nucleation of a new intermediate phase and atypical reaction pathway involving the hard carbon negative electrode, which could be contributing to the anomalous storage observed.[38–41] The voltage profiles in (Fig. S2) also support the trends observed in $\left(\frac{dQ}{dV}\right)$ analysis. At room temperature, both LIBs (Fig. S2a) and NIBs (Fig. S2b) show stable

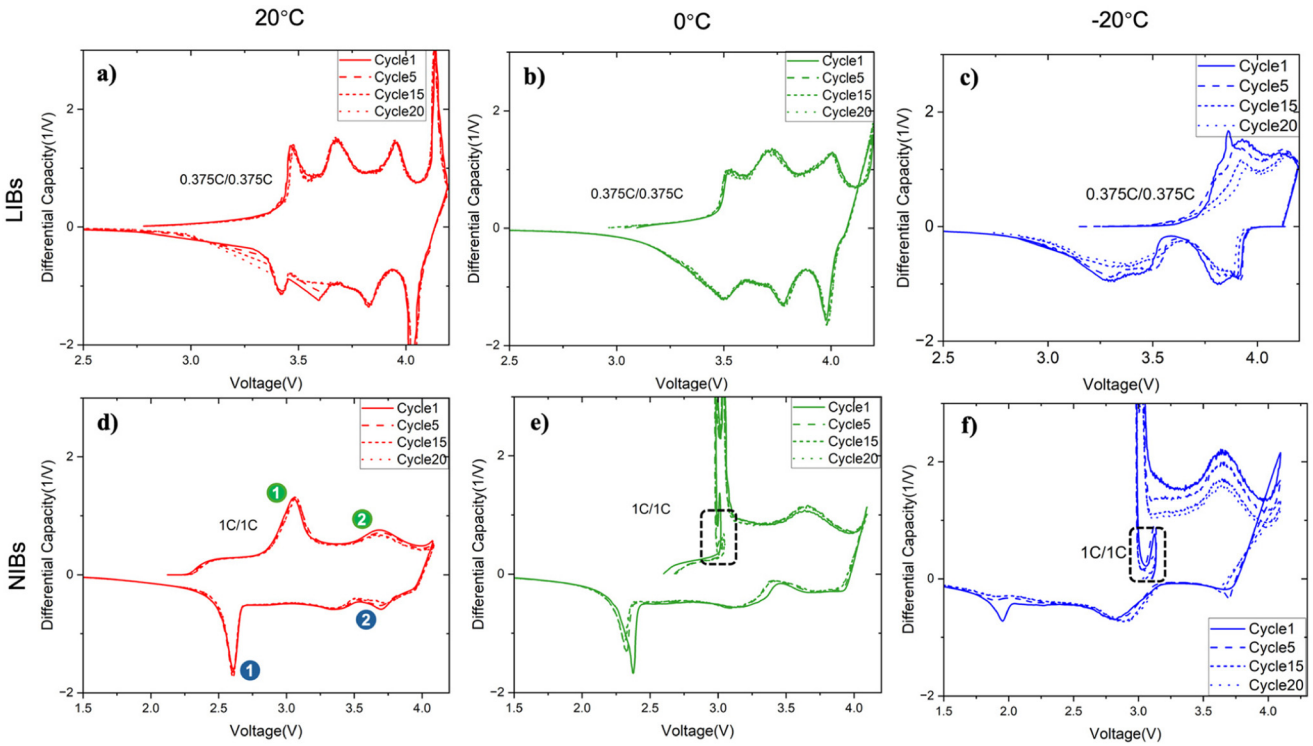

Fig. 3 Differential capacity curves across different cycles and temperatures: (a) LIB at 20 °C, (b) LIB at 0 °C, (c) LIB at −20 °C, (d) NIBs at 20 °C, (e) NIB at 0 °C, (f) NIB at −20 °C. (a) & (d) Illustrates the reversibility of voltage and capacity profiles as a function of cycle number, with LIBs showing distinct peaks for ion insertion while charging and discharging at the same voltages with cycling. This effect is less pronounced in NIBs due to the different electrode chemistry. (b), (c), (e) & (f) Highlight the evolution of specific voltage regions at low temperatures.

charge–discharge behavior with minimal voltage hysteresis. However, as the temperature drops to 0 °C and −20 °C, a clear voltage gap between the end of discharge and the start of charge emerges, particularly for NIBs (Fig. S2e & S2f), suggesting the system does not fully equilibrate. This behavior might be due in part to the lack of a rest period between charge and discharge.

To further study the effect of different temperatures on the peak shifts and charge capacity, we overlay the differential capacity curves from cycle 1. During charging, LIBs (Fig. 4a) exhibit peak shifts towards higher voltages as the temperature is lowered, an expected result considering the increased resistance at lower temperatures. However, for NIBs (Fig. 4c), the peaks remain largely unchanged. Instead, a sharp phase appears at the voltage range of ~3 V when charging at lower temperatures. This peak grows in prominence with decreasing temperatures. During discharge, this feature is not observed; instead, peaks 1, 2, and 3 at 20 °C, 0 °C, and −20 °C, respectively, shift to lower voltages. This shift is consistent with EIS measurements (Table S3) that show a much higher R_{SEI} and R_{ct} at lower temperatures. Under these conditions, NIBs show ~153× higher R_{ct} and ~69× higher R_{SEI} than LIBs. Moreover, NIBs exhibit ~31× higher R_{SEI} and ~3× higher R_{ct} during discharge than charge. This suggests that Na^+ must overcome a thick, resistive SEI which can be a potential contributor to the observed capacity hysteresis and will be discussed later in more detail.[42] Hence, both differential capacity analysis and EIS measurements reveal the expected resistance trends for LIBs. That is, LIBs exhibit peak shifts corresponding to temperature-dependent kinetics during charging and discharging, features which are not observed in NIBs.

The differential capacity curves were then analyzed to verify the anomalous capacity hysteresis ratio trends reported earlier using cycling data. Here, for LIBs (Fig. 4b), the integrated areas under the $\frac{dQ}{dV}$ curves decrease with lowering temperature, with the charge area reducing by ~40% and the discharge area by ~30% from 20 °C to −20 °C. In contrast, for NIBs (Fig. 4d), the area under the charge curve is larger than that under the discharge curve across all temperatures, with this difference becoming more pronounced as temperature decreases. Specifically, the charge integrated area increases by ~120% and the discharge integrated area decreases by ~20% from 20 °C to −20 °C. These computed areas under the curve are consistent with the anomalously large capacity hysteresis ratios previously observed for NIBs at low temperatures.

3.4. Comparing different manufacturers of NIBs

We investigated whether the capacity hysteresis behavior is universal across NIBs or specific to a particular manufacturer. To do this, we evaluated another commercially available NIB, Sriko 18650[43] ($Na_xNiMnFeO_2$|hard carbon|~93% carbonate

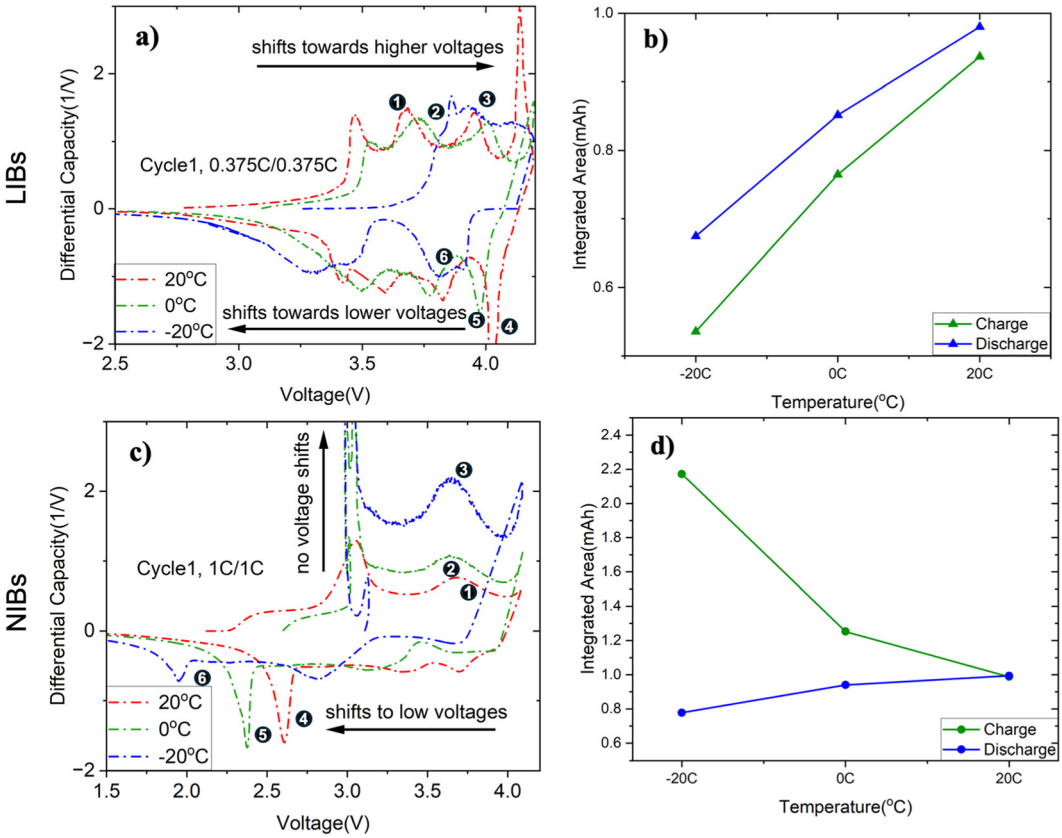

Fig. 4 Comparing the capacity curves of LIBs and NIBs at 20 °C, 0 °C and −20 °C: (a) no prominent voltage shifts are observed in LIBs. (b) The graph shows nearly constant changes in charge and discharge unlike NIBs. (c) The peak shifts were more prominent for NIBs while discharging than charging. (d) The graph illustrates that the area under the charge curve is more than the discharge curve, further suggesting the capacity hysteresis effect.

electrolyte abbreviated as NMF|HC|SC93), with a nominal capacity of 1200 mAh and voltage of 3 V and cut-off voltages of 4 V for charge and 2 V for discharge. Both cells were tested under identical conditions of 1C/1C charge/discharge, and performance metrics were studied using the same protocols across various temperatures. In terms of capacity hysteresis, Sriko cells measured at cycle 1 showed ratios of 2.05 ± 0.00 at −20 °C, 1.3 ± 0.19 at 0 °C, and 1.00 ± 0.00 at 20 °C. Unlike Hakadi cells, whose hysteresis increased with cycling, Sriko cells showed a decline reaching 1.73 ± 0.00 at −20 °C and 1.1 ± 0.09 at 0 °C (Fig. 5) by 80% SoH. In addition, we evaluated NaFR cells from another manufacturer with a nominal capacity of 1300 mAh and cut-off voltages of 3.95 V for charge and 2 V for discharge. Using the same 1C/1C protocol at −20 °C, these cells showed a similar phenomenon (Fig. S3). Overall, we confirmed that the large capacity hysteresis ratios are present for multiple NIB cell manufacturers, although the extent to which it exists varies. This observation provides further evidence that this anomalous phenomenon is a characteristic of the NIB chemistry rather than that of a particular NIB manufacturer. Similar temperature-dependent trends, with the ratio increasing at lower temperatures, also suggest a shared underlying mechanism across different NIB cell types.

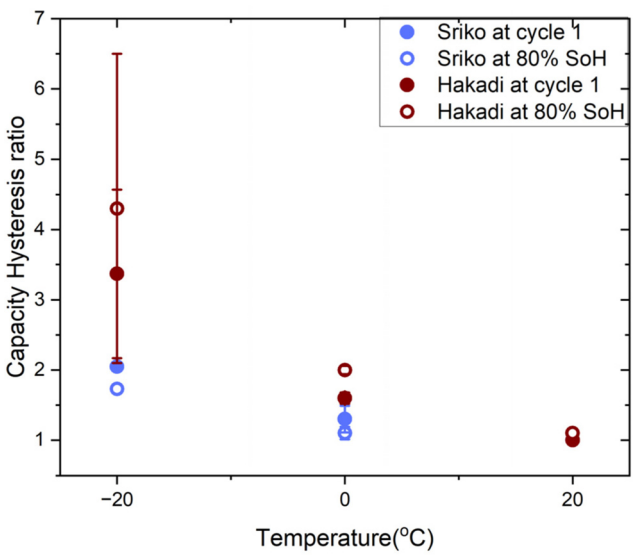

Fig. 5 Capacity hysteresis ratio for Sriko and Hakadi measured at −20 °C, 0 °C and 20 °C during the first cycle and at 80% SoH.

3.5. Post-mortem analysis

To identify the mechanism behind the anomalously large capacity hysteresis ratios in NIBs, we disassembled the cycled batteries to directly observe the electrodes. During fresh cell disassembly, no electrolyte was observed in LIBs (Fig. S4a), whereas a noticeably larger volume of electrolyte was present in NIBs (Fig. S4b). This excess amount of electrolyte may help explain the additional sodium supply during cycling at low temperatures and contribute to capacity hysteresis in NIBs. Furthermore, in cycled NIBs (80% SoH) at −20 °C, a striking difference was observed between the negative electrode surfaces (Fig. 6c and g). The Hakadi negative electrode showed clear evidence of a change in surface color to gray. We attribute this surface color change to sodium metal deposition since the material was soluble in dimethyl carbonate and reacted readily with water (Fig. S5). In addition, traces of leftover electrolyte were observed inside the battery can (Fig. S6a). Comparatively, the Sriko negative electrode did not show the same extent of sodium metal deposition even after cycling at −20 °C and nor did it show traces of electrolyte residue (Fig. S6b). This indicates that severe degradation mechanisms at the positive electrode, such as extensive oxygen loss or phase collapse, are unlikely to be the dominant source of the excess charge capacity under our cycling conditions.[44,45] However, no changes were observed on the positive electrode surfaces for either battery (Fig. S7). It is clear that if the negative electrode undergoes sodium metal deposition, the positive electrode must simultaneously undergo reactions beyond its normal intercalation/deintercalation. In fact, we observed clear evidence of corrosion on the inner surface of the battery can (Fig. S8).

The reaction pathway based on these observations is the following:Na metal formation at negative electrode side:

$$Na^{+} + e^{-} \rightarrow Na^{0}$$

Fe corrosion at can:

$$Fe \rightarrow Fe^{2+} + 2e^{-};\ Fe^{2+} \rightarrow Fe^{3+} + e^{-}$$

In this case, electrons are generated through parasitic oxidation at the battery can on the positive electrode side[46,47] which are consumed at the negative electrode side through the formation of Na metal. In addition to our observations, other reports have shown that battery can corrosion are commonly observed under low temperature and strong polarization conditions.[48] Moreover, ICP-MS and Raman Spectroscopy was used to confirm that positive electrode and negative electrode compositions of both cells were nominally identical as $Na_xNiMnFeO_2$ (NMF) (Fig. S9a) and hard carbon (HC), respectively (Fig. S9b). Additionally, Scanning Electron Microscope (SEM) of the negative electrode surface clearly highlighted morphological differences between the two negative electrodes (Fig. S10). However, after cycling, the Hakadi anode (Fig. 6d) did not show significant surface deposition like Fig. 6b, suggesting that the sodium metal deposition was mainly occurring within the pores of the hard carbon as a uniform layer, rather than on the surface. Consistent with this, EDS shows a clear increase in Na and O contents after cycling (Fig. S11). We also note that a Na signal is present on the fresh hard carbon negative electrodes, which we attribute to residual $NaPF_6$ salt from the electrolyte which is discussed in detail in the later section.

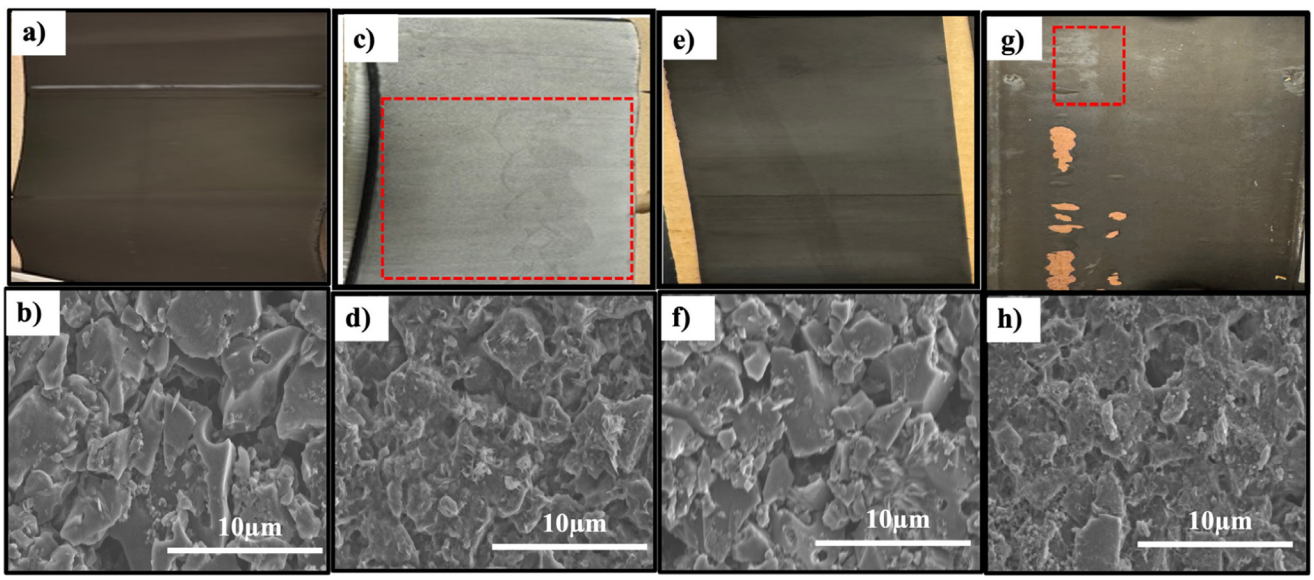

Fig. 6 Optical and SEM images of negative electrode surfaces before (100% SoH) and after (80% SoH) cycling at −20 °C: (a) optical image of Fresh Hakadi, (b) SEM image of Fresh Hakadi, (c) optical image of −20 °C Hakadi, (d) SEM image of −20 °C Hakadi, (e) optical image of Fresh Sriko, (f) SEM image of Fresh Sriko, (g) optical image of −20 °C Sriko, (h) SEM image of −20 °C Sriko.

3.6. Proposed mechanism of large low-temperature capacity hysteresis ratio

Based on the observations from cycle testing, differential capacity analysis, and post-mortem analysis, we propose that the anomalously large charge capacities measured at low temperatures can be primarily attributed to sodium metal deposition on the hard carbon negative electrode surface. At least two factors influence this deposition process:

3.6.1. Diffusion kinetics of Na at the hard carbon interface and within its pores. As shown schematically in Fig. 7a–d, at lower temperatures Na^+ does not always intercalate efficiently into the hard carbon structure.[38–40,49] Instead, some Na^+ intercalates as expected, while a portion is adsorbed and forms a thin, metallic homogenous layer. We speculate that this is because of the slower diffusion of Na^+ in the electrolyte at such low temperatures.[50–52] Na^+ transport across the interface proceeds in three main steps, 1. Na^+ in electrolyte is solvated by the solvent, 2. Solvated Na^+ then de-solvates at the electrode surface, and 3. Na^+ diffuses into the hard carbon. If any one of these steps is not fast enough, the de-solvated Na^+ may fail to intercalate into the hard carbon. In that case, it can absorb an electron and be reduced to Na^0, leading to sodium metal deposition within the pores of the disordered hard carbon.[53] Thus, a fraction of this deposited sodium likely becomes electrochemically inactive which is consistent with the increased R_{SEI} and R_{ct} observed in EIS (Table S3). We therefore hypothesize that the large capacity hysteresis observed (Fig. 1b and d) arises from the combined effect of partial adsorption and incomplete intercalation with hard carbon, along with side reactions at the interface. Furthermore, the early-stage nature of deposits observed after only five cycles (Fig. S12) suggests that this sodium metal accumulation does not require battery aging but shows up from the very beginning of cycling.

This interpretation is supported by the differential capacity analysis from section 3.3, where we observed the distinct growth of a new $\frac{dQ}{dV}$ peak between (3–4) V, but only while charging. Sodium metal deposition could explain this peak, a process that becomes more pronounced at lower temperatures, with larger intensity. The attribution of this peak to sodium metal deposition also implies a thermodynamic window in which this deposition is favorable in NIBs. Unlike lithium-ion systems, where lithium plating is largely driven by graphite saturation, sodium metal deposition can occur earlier due to sluggish Na^+ kinetics.

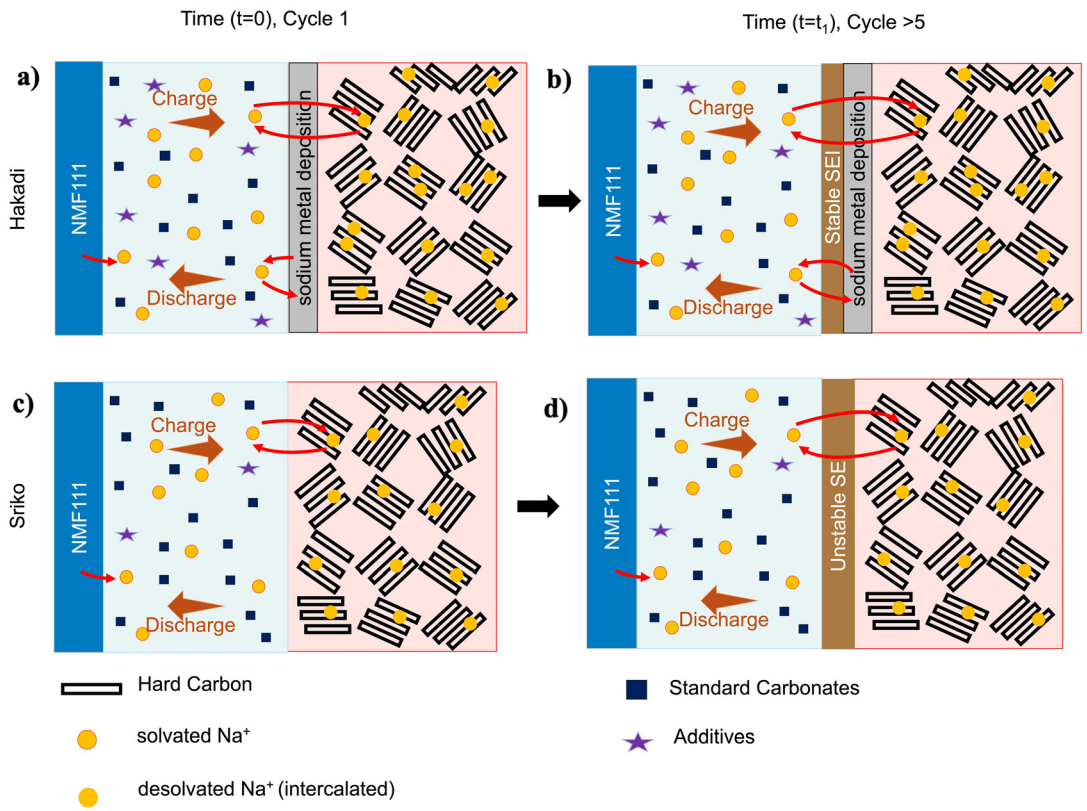

Fig. 7 Proposed mechanism demonstrating sodium diffusion limitations with hard carbon and the influence of electrolyte composition. (a) Hakadi at cycle 1, shows sodium metal deposition within the hard carbon electrode due to sluggish Na^+ kinetics at low temperatures, (b) after more than 5 cycles, Hakadi develops a stable SEI that regulates the interface, allowing sodium metal deposition to remain partially reversible and supporting extended cycling, attributed to its additive rich electrolyte, (c) Sriko at cycle 1 showing minimal sodium deposition (less visible in Optical and SEM images), despite the same NMF||HC chemistry, attributed to differences in surface chemistry, (d) Sriko showing rapid capacity fade and failing faster due to unstable SEI formation, linked to its carbonate rich electrolyte with fewer stabilizing additives.

We also hypothesize that differences in capacity hysteresis ratios between different NIB manufacturers are due in part to material structure differences in the hard carbon negative electrode, such as the degree of structural disorder. More specifically, the hard carbon negative electrode in Hakadi may undergo greater structural disorder under low temperature cycling. To test this hypothesis, Raman spectroscopy measurements were made to quantify I_D/I_G ratios,[49,53,54] a measure of structural disorder in carbon where ratios greater than one corresponds to increased disorder. Hakadi negative electrodes showed a marked increase from 1.07 (fresh) to 1.40 at −20 °C. In contrast, Sriko showed a smaller change from 1.24 (fresh) to 1.26 at −20 °C. This further suggests that Hakadi hard carbon is allowing more adsorption and intercalation,[38–40] consistent with the observed larger capacity hysteresis ratio.

3.6.2. Differences in electrolyte composition and quantity. We characterized NIB electrolytes using GC-MS technique,[55,56] observed the presence of Phosphoryl Fluoride (OPF_3) (Table S4), a known product of $NaPF_6$ salt decomposition followed by hydrolysis.[57] This confirms that both cells use the same $NaPF_6$ salt. However, the electrolyte compositions differ significantly: Hakadi contains a much lower amount of standard carbonates (SC) (~57%) (NMF|HC|SC57) compared to Sriko (~93%) (NMF|HC|SC93). While both cells shared a non-standard additive, thiolane-3,4-dicarbonitrile,2,5-di-*tert*-butyl-3,4-bis (trifluoromethyl), it is present in a higher amount for Hakadi (14.71 area %) compared to Sriko (7.07 area %). In addition, Hakadi's electrolyte includes two uncommon additives: 1,2-oxathilane,2,2-dioxide and 1,3-dioxolan-2-one,4-methyl. Based on this, we speculate that, despite the greater tendency for sodium metal to adsorb in hard carbon pores, the larger additive with lower carbonate concentration and larger electrolyte volume (Fig. S6a) is playing a key role in formation of a stable SEI layer. This could explain why Hakadi cells, though having higher capacity hysteresis ratios, still maintain a gradual capacity decline. In contrast, the electrolyte quantity (Fig. S6b) and formulation in Sriko may not be well suited to support stable cycling at low temperatures, resulting in capacity hysteresis during early cycles but leading to faster failure (Fig. 8).

Taken together, these results suggest a hypothesis of kinetics of sodium metal on hard carbon electrode at low-temperature, stable SEI formation, excess electrolyte volume and its non-standard electrolyte composition with fewer carbonates and more additives, all contributing to high charge capacity in Hakadi NIBs.

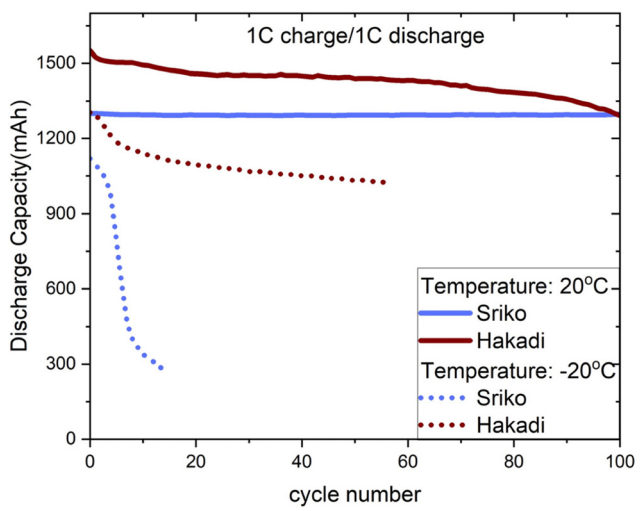

Fig. 8 Comparison of discharge capacity fade of Sriko and Hakadi at 20 °C and −20 °C.

4. Conclusion

Our work demonstrates that current COTS NIBs exhibit distinct electrochemical behaviors at 0 °C and below compared to LIBs. Features such as capacity hysteresis and voltage shifts are influenced by temperature-dependent and C-rate specific kinetic limitations. Importantly, this behavior appears to be a feature of commercial NIBs tested so far, with its extent determined by factors such as electrolyte composition and the degree of disorder in the hard carbon. Ongoing research is being conducted to study coin cell testing using electrodes harvested from Hakadi and Sriko cells but paired with different electrolyte compositions at various temperatures. We are also testing additional manufacturers and building a comparative database to understand the different trends. In parallel, we are working to understand the mechanisms behind capacity hysteresis in the lab by constructing NIBs with controlled combinations of negative electrode, positive electrode, and electrolyte. The goal is to guide future improvements in electrolyte and electrode design and help determine the appropriate chemistry behind this anomalous behavior. Several opportunities remain to better understand and optimize NIB performance under extremely low-temperature conditions.

Conflicts of interest

The authors declare no conflicts of interests.

Data availability

The data that support the findings of this study are available from the corresponding author upon reasonable request.

Supplementary information (SI) is available. See DOI: https://doi.org/10.1039/d5eb00185d.

Acknowledgements

We acknowledge funding support from the NATO Science for Peace and Society under proposal G6111: "Batteries for Low-temperature Operation < 0C (B-LO Zero)". This material is based upon work supported by the Department of Energy National Nuclear Security Administration under Award

Number DE-MS0000092. This material is based upon work supported by the National Science Foundation under Grant No. 2339233. We acknowledge resources and support from the Advanced Electronics and Photonics Core Facility at Arizona State University. We also acknowledge the use of facilities within the Eyring Materials Center at Arizona State University supported in part by NNCI-ECCS-1542160. Finally, we acknowledge Shimadzu Inc. for GC-MS measurements and analysis.

References

1 K. M. Abraham, How Comparable Are Sodium-Ion Batteries to Lithium-Ion Counterparts?, *ACS Energy Lett.*, 2020, **5**, 3544–3547, DOI: 10.1021/acsenergylett.0c02181.
2 N. Yabuuchi, K. Kubota, M. Dahbi and S. Komaba, Research development on sodium-ion batteries, *Chem. Rev.*, 2014, **114**, 11636–11682.
3 V. Palomares, P. Serras, I. Villaluenga, K. B. Hueso, J. Carretero-González and T. Rojo, Na-ion batteries, recent advances and present challenges to become low cost energy storage systems, *Energy Environ. Sci.*, 2012, **5**, 5884–5901.
4 L. Zhao, T. Zhang, W. Li, T. Li, L. Zhang, X. Zhang and Z. Wang, Engineering of Sodium-Ion Batteries: Opportunities and Challenges, *Engineering*, 2023, **24**, 172–183, DOI: 10.1016/j.eng.2021.08.032.
5 Z. Bai, Q. Yao, M. Wang, W. Meng, S. Dou, H. K. Liu and N. Wang, Low-temperature sodium-ion batteries: challenges and progress, *Adv. Energy Mater.*, 2024, **14**, 2303788, DOI: 10.1002/aenm.202303788.
6 R. R. Samigullin, O. A. Drozhzhin and E. V. Antipov, Comparative study of the thermal stability of electrode materials for Li-ion and Na-ion batteries, *ACS Appl. Energy Mater.*, 2021, **5**, 14–19.
7 F. Ngila, Chicago shows Teslas struggle in cold weather, *Quartz*, 2024, 1851172536.
8 S. G. Yoon, K. A. Cavallaro, B. J. Park, H. Yook, J. W. Han and M. T. McDowell, Controlling Solvation and Solid–Electrolyte Interphase Formation to Enhance Lithium Interfacial Kinetics at Low Temperatures, *Adv. Funct. Mater.*, 2023, **33**, 2302778.
9 Q. Li, G. Liu, H. Cheng, Q. Sun, J. Zhang and J. Ming, Low–temperature electrolyte design for lithium–ion batteries: prospect and challenges, *Chem. – Eur. J.*, 2021, **27**, 15842–15865.
10 X. Lin, K. Khosravinia, X. Hu, J. Li and W. Lu, Lithium plating mechanism, detection, and mitigation in lithium-ion batteries, *Prog. Energy Combust. Sci.*, 2021, **87**, 100953.
11 H. Laufen, S. Klick, H. Ditler, K. L. Quade, A. Mikitisin, A. Blömeke, M. Schütte, D. Wasylowski, M. Sonnet and L. Henrich, Multi-method characterization of a commercial 1.2 Ah sodium-ion battery cell indicates drop-in potential, *Cell Rep. Phys. Sci.*, 2024, **5**, 101945.
12 L. Luo, K. Chen, H. Chen, H. Li, R. Cao, X. Feng, W. Chen, Y. Fang and Y. Cao, Enabling Ultralow–Temperature (−70° C) Lithium–Ion Batteries: Advanced Electrolytes Utilizing Weak–Solvation and Low–Viscosity Nitrile Cosolvent, *Adv. Mater.*, 2024, **36**, 2308881.
13 H. Luo, Y. Wang, Y.-H. Feng, X.-Y. Fan, X. Han and P.-F. Wang, Lithium-ion batteries under low-temperature environment: challenges and prospects, *Materials*, 2022, **15**, 8166.
14 T. Yang, Y. Zheng, Y. Liu, D. Luo, A. Yu and Z. Chen, Reviving low-temperature performance of lithium batteries by emerging electrolyte systems, *Renewables*, 2023, **1**, 2–20.
15 J. Xu, J. Zhang, T. P. Pollard, Q. Li, S. Tan, S. Hou, H. Wan, F. Chen, H. He and E. Hu, Electrolyte design for Li-ion batteries under extreme operating conditions, *Nature*, 2023, **614**, 694–700.
16 C. Wang, Electrolyte design for ultra-stable, low-temperature lithium-ion batteries, *Matter*, 2023, **6**, 2610–2612.
17 Y. Lu, L. Li, Q. Zhang, Z. Niu and J. Chen, Electrolyte and interface engineering for solid-state sodium batteries, *Joule*, 2018, **2**, 1747–1770.
18 M. Wang, Q. Wang, X. Ding, Y. Wang, Y. Xin, P. Singh, F. Wu and H. Gao, The prospect and challenges of sodium–ion batteries for low–temperature conditions, *Interdiscip. Mater.*, 2022, **1**, 373–395.
19 X. Qiu, Y. Chen, Y. Sun, Y. Wang, Z. Liang, G. Zhou, Y. Xue, L. Shi, J. Jiang and X. Kong, Research on Low-Temperature Sodium-Ion Batteries: Challenges, Strategies and Prospect, *Energy Storage Mater.*, 2024, 103760.
20 Molicel INR21700P42A-V4-80092.
21 Selian (Hakadi) HKD-18650-3V_1500.
22 S. S. Margoschis, *State-of-Health Characterization to Estimate Battery Degradation for Second-Life Applications*, Arizona State University, 2024.
23 M. Dubarry and G. Baure, Perspective on commercial Li-ion battery testing, best practices for simple and effective protocols, *Electronics*, 2020, **9**, 152.
24 M. Dubarry, B. Y. Liaw, M.-S. Chen, S.-S. Chyan, K.-C. Han, W.-T. Sie and S.-H. Wu, Identifying battery aging mechanisms in large format Li ion cells, *J. Power Sources*, 2011, **196**, 3420–3425.
25 M. Dubarry, V. Svoboda, R. Hwu and B. Y. Liaw, Incremental capacity analysis and close-to-equilibrium OCV measurements to quantify capacity fade in commercial rechargeable lithium batteries, *Electrochem. Solid-State Lett.*, 2006, **9**, A454.
26 EIS_Bio-Logic EC-Lab Application Note.
27 P. Křivík, Impedance changes of the Li-ion cell in the course of discharge, *Monatsh. Chemie*, 2024, **155**, 237–243, DOI: 10.1007/s00706-024-03175-7.
28 Y. Zhao, Z. Zhang, Y. Zheng, Y. Luo, X. Jiang, Y. Wang, Z. Wang, Y. Wu, Y. Zhang and X. Liu, Sodium-Ion Battery at Low Temperature: Challenges and Strategies, *Nanomaterials*, 2024, **14**, 1604.
29 J. F. Nilsson, *Low temperature Li-ion battery ageing*, 2014.
30 Y. Yang, L. Zhao, Y. Zhang, Z. Yang, W. Lai, Y. Liang, S. Dou, M. Liu and Y. Wang, Challenges and Prospects of Low–Temperature Rechargeable Batteries: Electrolytes, Interfaces, and Electrodes, *Adv. Sci.*, 2024, **11**, 2410318.

31 T. R. Jow, S. A. Delp, J. L. Allen, J.-P. Jones and M. C. Smart, Factors limiting Li+ charge transfer kinetics in Li-ion batteries, *J. Electrochem. Soc.*, 2018, **165**, A361.
32 B. Xu, D. Qian, Z. Wang and Y.S. Meng, Recent progress in cathode materials research for advanced lithium ion batteries, *Mater. Sci. Eng. R Rep.*, 2012, **73**, 51–65.
33 N. Nitta, F. Wu, J. T. Lee and G. Yushin, Li-ion battery materials: Present and future, *Mater. today*, 2015, **18**, 252–264, DOI: 10.1016/j.mattod.2014.10.040.
34 I. Landa-Medrano, A. Eguia-Barrio, S. Sananes-Israel, S. Lijó-Pando, I. Boyano, F. Alcaide, I. Urdampilleta and I. de Meatza, In Situ Analysis of NMC|graphite Li-Ion Batteries by Means of Complementary Electrochemical Methods, *J. Electrochem. Soc.*, 2020, **167**, 090528, DOI: 10.1149/1945-7111/ab8b99.
35 W. Wang, Y. Sun, P. Wen, Y. Zhou and D. Zhang, Enhanced conduction and phase transition reversibility of O3-type NaNi1/3Fe1/3Mn1/3O2 cathode via Ta doping for high-performance sodium-ion battery, *J. Energy Storage*, 2024, **79**, 110177, DOI: 10.1016/j.est.2023.110177.
36 C. Zhao, Y. Wei, Y. Pan and C. Chen, A novel strategy for capacity judgement of hard carbon in sodium-ion batteries: Ensuring the consistency of the available anode capacity between half-cell and full-cell, *Solid State Ionics*, 2024, **412**, 116586, DOI: 10.1016/j.ssi.2024.116586.
37 Y. Xie, H. Gao, R. Harder, L. Li, J. Gim, H. Che, H. Wang, Y. Ren, X. Zhang, L. Li, *et al.*, Revealing the Structural Evolution and Phase Transformation of O3-Type NaNi1/3Fe1/3Mn1/3O2Cathode Material on Sintering and Cycling Processes, *ACS Appl. Energy Mater*, 2020, **3**, 6107–6114, DOI: 10.1021/acsaem.0c00475.
38 H. Sun, Q. Zhang, Y. Ma, Z. Li, D. Zhang, Q. Sun, Q. Wang, D. Liu and B. Wang, Unraveling the mechanism of sodium storage in low potential region of hard carbons with different microstructures, *Energy Storage Mater.*, 2024, **67**, 103269, DOI: 10.1016/j.ensm.2024.103269.
39 X. Chen, C. Liu, Y. Fang, X. Ai, F. Zhong, H. Yang and Y. Cao, Understanding of the sodium storage mechanism in hard carbon anodes, *Carbon Energy*, 2022, **4**, 1133–1150, DOI: 10.1002/cey2.196.
40 J. Wang, L. Xi, C. Peng, X. Song, X. Wan, L. Sun, M. Liu and J. Liu, Recent Progress in Hard Carbon Anodes for Sodium-Ion Batteries, *Adv. Eng. Mater.*, 2024, **26**, 2302063, DOI: 10.1002/adem.202302063.
41 X. Fan, X. Kong, P. Zhang and J. Wang, Research progress on hard carbon materials in advanced sodium-ion batteries, *Energy Storage Mater*, 2024, **69**, 103386.
42 M. Sai Bhargava Reddy, D. Jeong, S. Aich and V. G. Pol, Low-temperature sodium-ion batteries: challenges, engineering strategies, safety considerations, and future directions, *EES Batteries*, 2025, **1**, 1444–1480, DOI: 10.1039/d5eb00121h.
43 Sriko Na-ion Cell Specification.
44 Y. Kuang, Y. Wu, H. Zhang and H. Sun, Interface Issues of Layered Transition Metal Oxide Cathodes for Sodium-Ion Batteries: Current Status, Recent Advances, Strategies, and Prospects, *Molecules*, 2024, **29**, 5988, DOI: 10.3390/molecules29245988.
45 C. Li, F. Geng and B. Hu, Anionic redox in Na-based layered oxide cathodes: a review with focus on mechanism studies, *Mater. Today Energy*, 2020, **17**, 100474, DOI: 10.1016/j.mtener.2020.100474.
46 F. Xu, H. He, Y. Liu, C. Dun, Y. Ren, Q. Liu, M. Wang and J. Xie, Failure Investigation of LiFePO 4 Cells under Overcharge Conditions, *J. Electrochem. Soc.*, 2012, **159**, A678–A687, DOI: 10.1149/2.024206jes.
47 D. Stephens, P. Shawcross, G. Stout, E. Sullivan, J. Saunders, S. Risser and J. Sayre, *Lithium-ion Battery Safety Issues for Electric and Plug-in Hybrid Vehicles*, National Highway Traffic Safety Administration, Washington, DC, 2017.
48 J. Zhang, R. Zhang, F. Duan, M. Niu, G. Zhang, T. Huang, X. Wang, Y. Wen, N. Xu and X. Liu, Influence of Overcharge Abuse on the Thermal-Electrochemical Performance of Sodium Ion Cells, *Energies*, 2025, **18**, 3580, DOI: 10.3390/en18133580.
49 Z. Zhou, Z. Wang, Y. Zhang, Q. Lin, Y. Shuai and L. Fan, Rational design of hard carbon anodes for sodium-ion batteries: Precursor engineering, structural modulation and industrial scalability, *Energy Storage Mater.*, 2025, **80**, 104443, DOI: 10.1016/j.ensm.2025.104443.
50 X. Qiu, Y. Chen, Y. Sun, Y. Wang, Z. Liang, G. Zhou, Y. Xue, L. Shi, J. Jiang, X. Kong, *et al.*, Research on low-temperature sodium-ion batteries: Challenges, strategies and prospect, *Energy Storage Mater.*, 2024, **72**, 103760, DOI: 10.1016/j.ensm.2024.103760.
51 M. Li, H. Zhuo, Q. Jing, Y. Gu, Z. Liao, K. Wang, J. Hu, D. Geng, X. Sun and B. Xiao, Low-temperature performance of Na-ion batteries, *Carbon Energy*, 2024, **6**, e546, DOI: 10.1002/cey2.546.
52 L. Wang, N. Ren, H. Yang, Y. Yao and Y. Yu, Advances in low-temperature electrolytes for sodium-ion batteries, *Energy Storage Science and Technology*, 2024, **13**, 2206–2223, DOI: 10.19799/j.cnki.2095-4239.2024.0376.
53 H. Zhou, Y. Song, B. Zhang, H. Sun, I. A. Khurshid, Y. Kong, L. Chen, L. Cui, D. Zhang, W. Wang, *et al.*, Overview of electrochemical competing process of sodium storage and metal plating in hard carbon anode of sodium ion battery, *Energy Storage Mater.*, 2024, **71**, 103645, DOI: 10.1016/j.ensm.2024.103645.
54 A. Merlen, J. G. Buijnsters and C. Pardanaud, A guide to and review of the use of multiwavelength Raman spectroscopy for characterizing defective aromatic carbon solids: From graphene to amorphous carbons, *Coatings*, 2017, **7**, 153, DOI: 10.3390/coatings7100153.
55 Y. Nagao, N. L. Parodi, W. Weber and X. Mönnighoff, *GC/MS Analysis of Fluorophosphates as Decomposition Products in Lithium Battery Electrolyte*, Application News No. 05-SCA-280-105-EN, Shimadzu Corporation, 2024.
56 V. Kraft, P. Jochems, B. Bollig, R. Ludwig and G. J. Schad, *User Benefits Application News Analysis of Fluoride in LiPF 6-based Li Ion Battery Electrolytes by Column-Switching Ion Chromatography, Fast and sensitive analysis of fluoride and related anionic products in Li ion battery electrolytes, Organic modifiers in the eluent for elution of strongly retarded hexa-*

fluorophosphate not required, Analysis of hexafluorophosphate in simple electrolyte compositions possible, 2021.

57 P. Barnes, K. Smith, R. Parrish, C. Jones, P. Skinner, E. Storch, Q. White, C. Deng, D. Karsann, M. L. Lau, *et al.*, A non-aqueous sodium hexafluorophosphate-based electrolyte degradation study: Formation and mitigation of hydrofluoric acid, *J. Power Sources*, 2020, **447**, 227363, DOI: 10.1016/j.jpowsour.2019.227363.